Bioconvection in spatially extended domains

A. Karimi

Department of Engineering Science and Mechanics, Virginia Polytechnic Institute and State University, Blacksburg, Virginia 24061, USA

M. R. Paul

Department of Mechanical Engineering, Virginia Polytechnic Institute and State University, Blacksburg, Virginia 24061, USA

We numerically explore gyrotactic bioconvection in large spatially extended domains of finite depth using parameter values from available experiments with the unicellular alga *Chlamydomonas nivalis*. We numerically integrate the three-dimensional, time-dependent continuum model of Pedley *et al.* [J. Fluid Mech. **195**, 223 (1988)] using a high-order, parallel, spectral-element approach. We explore the long-time nonlinear patterns and dynamics found for layers with an aspect ratio of 10 over a range of Rayleigh numbers. Our results yield the pattern wavelength and pattern dynamics which we compare with available theory and experimental measurement. There is good agreement for the pattern wavelength at short times between numerics, experiment, and a linear stability analysis. At long times we find that the general sequence of patterns given by the nonlinear evolution of the governing equations correspond qualitatively to what has been described experimentally. However, at long times the patterns in numerics grow to larger wavelengths, in contrast to what is observed in experiment where the wavelength is found to decrease with time.

PACS number(s): 47.54.−r, 47.20.Bp, 47.63.Gd, 87.18.Hf

I. INTRODUCTION

The collective motion of many microorganisms in a fluid environment is an ubiquitous phenomenon of nature and is an important feature of a broad range of important systems. It is a common feature of oceans, streams, and lakes and occurs in fluids contained within animals [1]. For example, the large-scale motion of vast quantities of phytoplankton in the oceans plays an important role in climate models via their production of cloud-condensation nuclei which are central to descriptions of the global thermostat (c.f. [2,3]). In addition, swimming microorganisms such as algae, bacteria, protozoa, and spermatozoa can form suspensions with complex collective dynamics that play a vital role in the organism's life cycle and its impact upon its surroundings [1,4].

In this paper we focus our attention on what is called bioconvection, which is a general term used to describe the pattern formation caused by the upward swimming of many microorganisms in a fluid [1,5]. Free-swimming microorganisms often swim with a particular direction relative to the variation of an external stimulus. Examples include chemical gradients (chemotaxis), variations in light intensity (phototaxis), a gravitational field (gravitaxis), and variations in the rheological properties of the surrounding fluid (rheotaxis). The study of these *taxes* and others has a rich and growing literature [1].

In this study we are interested in gyrotactic microorganisms that are slightly denser than water with an asymmetrical mass distribution. The cells are bottom heavy where the center of mass is below the geometrical center. In the limit of small Reynolds number flow where inertia is negligible, the swimming microorganisms balance the viscous torque with a gravitational torque which results in an upward swimming direction at some angle with the vertical.

We will focus our attention on the microorganism *Chlamydomonas nivalis*. *C. nivalis* is a unicellular, freshwater, and biflagellate swimming green alga [6]. The swimming stroke consists of a breast-stroke motion of its two anterior flagella. Geometrically it is a prolate spheroid with a typical length of approximately 10 μm and typical swimming speed of 70 μm/s. It is about 5% more dense than water. Using these typical parameters yields a Reynolds number for the flow field caused by a swimming microorganism of Re $\approx 7 \times 10^{-4} \ll 1$ and is essentially inertia free.

There are many experiments discussed in the literature that present the striking patterns of bioconvection for a variety of different suspensions of swimming microorganisms [1,6–10]. Typically, the experiments are conducted in large shallow containers with aspect ratios $\Gamma = L/H \gg 1$, where L is the length of the domain and H is the depth of the fluid layer. The experimental images are photographs taken from above where the light intensity can be related qualitatively with the spatial variation of the local concentration of the microorganisms at the top of the suspension. In this paper we will focus our attention upon the experiments of Bees and Hill [6]; typical experimental bioconvection patterns can be seen in Figs. 2–4 of this reference.

There has been significant progress modeling the complex processes that result in bioconvection. The first models were continuous and deterministic and assumed dilute suspensions of microorganisms whose swimming results in low Reynolds number flow [8,9,11]. The inherent randomness present in a population of swimming cells was modeled as deterministic diffusion. A linear stability analysis yielded predictions for the wavelength describing bioconvection that were found to be approximately 5 times too large when compared with long-time experimental measurements [11,12].

Subsequent efforts included stochastic effects by allowing the swimming direction to be a random process. Pedley and Kessler [13] included a Fokker-Planck equation for the probability density function representing the swimming directions of the microorganisms. A linear stability analysis of this model for the wavelength of the bioconvection also

yielded wavelengths larger than the experimentally measured values and was very similar to the result using the purely deterministic model of Ref. [11]. Hill and Häder [14] modeled bioconvection as the continuous limit of a correlated and biased random walk. In this work, both gravitaxis and phototaxis were explored and the model was used with careful experimental measurements to quantify macroscopic quantities of potential interest to theoretical modeling efforts.

There have been a number of numerical explorations of bioconvection. Ghorai and Hill [15,16] have performed a series of numerical simulations using the continuous and deterministic model of Ref. [11]. Initially, two-dimensional bioconvection in deep chambers was explored [15]. More recently [16], full three-dimensional bioconvection was numerically explored in a small aspect ratio domain capable of supporting a single bioconvection plume.

There have been efforts to perform numerical simulations of bioconvection that include stochastic effects as well as the discrete nature of the individual microorganisms. Hopkins and Fauci [17] accounted numerically for the discrete microorganisms as point sources of gravitational force in the governing equations for the fluid motion. In this work two-dimensional bioconvection was explored for gyrotactic and chemotactic microorganisms and yielded long-time patterns resembling those of experiment.

In this paper we are interested in the long-time nonlinear evolution of the bioconvection patterns in spatially extended domains that are typical in experiment. We use the deterministic and continuous model of Pedley *et al.* [11] and perform large-scale parallel numerical simulations for parameter values relevant to the experiments of Bees and Hill [6]. We exploit the significant progress of computational research on Rayleigh-Bénard convection in large domains (c.f. [18,19]) to perform long-time numerical simulations of bioconvection in large spatially extended domains. We are particularly interested in quantifying the pattern dynamics in the nonlinear regime and its comparison with experimental observations.

II. APPROACH

A. Mathematical formulation

In the following we only provide the essential ideas to describe the model; for more details see Ref. [11]. The number density or concentration of the cells is given by $n(\mathbf{x},t)$, where $\mathbf{x} = (x,y,z)$ represents the spatial coordinates in a Cartesian reference frame and t is the time. For a dilute suspension of cells $nv \ll 1$, where v is the average volume of a single cell. The conservation of momentum and mass for the fluid suspension in dimensional form yields

$$\rho \frac{\partial \mathbf{u}}{\partial t} + \rho \mathbf{u} \cdot \nabla \mathbf{u} = -\nabla p_e - nv\Delta\rho\, g\hat{\mathbf{z}} + \mu\nabla^2\mathbf{u}, \quad (1)$$

$$\nabla \cdot \mathbf{u} = 0, \quad (2)$$

where p_e is the pressure excess over hydrostatic, g is the acceleration due to gravity, $\hat{\mathbf{z}}$ is a unit vector opposing gravity, μ is the dynamic viscosity of the fluid, ρ is the fluid density, and $\rho + \Delta\rho$ is the mean cell density, where $\Delta\rho$ is approximately 5% larger than ρ in typical experiments. The second to last term on the right-hand side of Eq. (1) represents the Boussinesq

approximation by allowing density variations in the buoyancy term. Equation (2) is for an incompressible fluid and yields a divergence-free velocity field.

The equation for the cell concentration is given by the conservation of the number of cells. It is typical to neglect birth and death processes which occur on time scales longer than those that describe the dynamics of bioconvection. In addition, the sedimentation velocity is much smaller than the swimming velocity and can also be neglected. The resulting dimensional equation is

$$\frac{\partial n}{\partial t} = -\nabla \cdot \mathbf{J}, \quad (3)$$

where the flux of the cells $\mathbf{J}$ is given by

$$\mathbf{J} = n\mathbf{u} + nW_c\mathbf{p} - D\nabla n, \quad (4)$$

where D is the isotropic diffusion coefficient for the cells, W_c is the constant cell swimming speed, and $\mathbf{p}$ represents the unit vector of the orientation of the cells.

The algal cells are known to be slightly ellipsoidal in geometry with typical values of cell eccentricity of $\alpha_0 \approx 0.3$ [12]. In our analysis we will proceed with the assumption that the cells are spherical where $\alpha_0 = 0$ and have a radius a and mass m. The cells are bottom-heavy with a distance h between the center of mass and the geometric center. In the limit of low Reynolds number the balance of the gravitational and viscous torques yields an expression for the time variation of the orientation of a swimming cell [16],

$$\frac{d\mathbf{p}}{dt} = \frac{1}{2B}[\hat{\mathbf{z}} - (\hat{\mathbf{z}} \cdot \mathbf{p})\mathbf{p}] + \frac{1}{2}\boldsymbol{\omega} \times \mathbf{p}, \quad (5)$$

where the vorticity is $\boldsymbol{\omega} = \nabla \times \mathbf{u}$ and the time scale of reorientation is given by the gyrotactic reorientation parameter,

$$B = \frac{4\pi\mu a^3}{mgh}. \quad (6)$$

It will be insightful to proceed by nondimensionalizing Eqs. (1)–(5). We will follow the convention of using the depth of the layer H as the length scale, the time required for a cell to diffuse across the layer depth H^2/D as the time scale, the quantity $\rho D^2/H^2$ as the pressure scale, and the mean cell concentration $\bar{n}$ as the concentration scale [16]. The governing nondimensional equations are

$$\frac{\partial \mathbf{u}}{\partial t} + \mathbf{u} \cdot \nabla \mathbf{u} = -\nabla p_e + S\nabla^2\mathbf{u} - SRn\hat{\mathbf{z}}, \quad (7)$$

$$\frac{\partial n}{\partial t} + \mathbf{u} \cdot \nabla n = -\nabla \cdot (nV_c\mathbf{p}) + \nabla^2 n, \quad (8)$$

$$\nabla \cdot \mathbf{u} = 0. \quad (9)$$

The nondimensional equation for the cell orientation is given by

$$\frac{d\mathbf{p}}{dt} = \frac{1}{2G}[\hat{\mathbf{z}} - (\hat{\mathbf{z}} \cdot \mathbf{p})\mathbf{p}] + \frac{1}{2}\boldsymbol{\omega} \times \mathbf{p}. \quad (10)$$

These equations contain several important nondimensional parameters. The Schmidt number

$$S = \frac{v}{D} \quad (11)$$

represents a ratio of the diffusion of momentum to the diffusion of cells where where $\nu = \mu/\rho$ is the kinematic viscosity of the suspension. The Rayleigh number

$$R = \frac{\bar{n} \nu \Delta \rho g H^3}{\rho \nu D} \qquad (12)$$

represents the ratio of buoyancy to viscous forces. The scaled swimming speed is

$$V_c = \frac{W_c}{D/H}, \qquad (13)$$

where the swimming velocity is normalized by a mass diffusion velocity scale. The scaled swimming velocity can also be interpreted as a ratio of length scales d, where $d = V_c$ and is the ratio of the suspension depth to a length scale describing the equilibrium concentration of microorganisms located near the top surface [12]. For $d \gg 1$ the suspension can be described as a deep layer and for $d \ll 1$ the suspension is a shallow layer. Lastly, the dimensionless gyrotactic number

$$G = \frac{B}{H^2/D} \qquad (14)$$

represents the ratio of the time scale of reorientation to the diffusion time scale.

B. Numerical procedure

There has been significant progress in the numerical simulation of bioconvection. From very early on, the qualitative connection of bioconvection with the fluid motion of Rayleigh-Bénard convection has been observed [5]. Rayleigh-Bénard convection is the fluid motion that results when a shallow layer of fluid is heated from below in an opposing gravitation field. As the temperature difference across the fluid layer increases, buoyancy eventually overcomes viscosity, resulting in patterns of convection cells. Rayleigh-Bénard convection is a canonical pattern forming system where significant progress has been made in improving our physical understanding of the dynamics of systems driven far from equilibrium [20,21].

To solve the system of equations given by Eqs. (7)–(10), we used a highly efficient, high-order, parallel, spectral-element approach that has been developed to solve the Boussinesq equations (c.f. [18]). The numerical approach has been used to explore a number of fundamental questions for Rayleigh-Bénard convection in large shallow domains for the precise conditions of experiment [22–25].

In our numerical simulations we use a box geometry with a solid bottom and a free surface at the top of layer. For the sidewalls we have explored both the cases of solid sidewalls and periodic sidewall boundary conditions. At all material surfaces we impose the no-slip velocity boundary condition and the free surface has zero shear stress. For the case of solid sidewalls we enforce a no-flux boundary condition for the concentration of the cells on all boundaries,

$$\mathbf{J} \cdot \hat{\mathbf{n}} = 0, \qquad (15)$$

where $\hat{\mathbf{n}}$ is the outward pointing unit normal with respect to a boundary. For the case of periodic sidewall boundary conditions, the fluid velocity and the concentration of cells are periodic in the horizontal directions.

In the numerical simulations, the initial conditions are a spatially uniform concentration field for the cells upon which we have added a small random perturbation,

$$n(\mathbf{x}, t = 0) = 1 + \epsilon \delta(\mathbf{x}), \qquad (16)$$

where $\epsilon = 10^{-8}$ is the small magnitude of the perturbation and $0 \leqslant \delta(\mathbf{x}) \leqslant 1$ is a random number selected from a uniform distribution at each location in space.

Our approach is high order and uses an exponentially convergent spectral element discretization in space that can asymptotically achieve higher accuracy for a given number of numerical degrees of freedom than a finite element or finite difference code [26]. The code uses a stable third-order-accurate semi-implicit (operator splitting) discretization in time that allows time steps corresponding to Courant-Friedrichs-Lewy numbers in excess of unity [27]. A typical value of the numerical time step used in our calculations is $\Delta t = 10^{-4}$. The elliptic problems arising from the viscous and pressure substeps of the time integrator are solved iteratively with a multigrid preconditioned conjugate gradient method [28,29]. The code is highly optimized for parallel architectures and readily scales to thousands of processors.

III. RESULTS AND DISCUSSION

A. Comparison with experiment

We have chosen the parameters in our numerical simulations to correspond with the experimental investigation of Bees and Hill [6]. These experiments were conducted using *C. nivalis* for a range of conditions. Thirty-nine experiments were conducted in circular Petri dishes with a typical radius of $r_0 = 2.5$ cm with varying depths H of fluid suspension to yield aspect ratios of $3 \lesssim \Gamma_c \lesssim 21$. For cylindrical geometries it is common to define the aspect ratio as $\Gamma_c = r_0/H$. These experiments are for weakly gyrotactic suspensions of moderate depth that cover a broad range of Rayleigh numbers where $G \approx 0.02 \ll 1$, $d \approx 10$, and $95 \leqslant R \leqslant 3500$.

We initially focus our attention on experiments (17)–(19) in Ref. [6] as a representative example of experimental bioconvection. The experimental parameters are shown in Table I. Using the parameters of Table I with the typical properties of *C. nivalis* given in Ref. [16] yields the nondimensional parameters listed in Table II using Eqs. (11)–(14). The fluid properties for water are used where the density $\rho = 1000$ kg/m^3 and the dynamic viscosity $\mu = 1 \times 10^{-3}$ kg/m s. The isotropic diffusion coefficient for the microorganisms is $D = 5 \times 10^{-8}$ m^2/s, the ratio of the cell density to the density of water $\Delta \rho / \rho = 0.05$, the average swimming speed of a cell

TABLE I. Experimental parameters used by Bees and Hill [6] to study the bioconvection of *C. nivalis* upon which we have based our numerical simulations. r_0 is the radius of the cylindrical Petri dish, H is the depth of the fluid suspension, $\bar{n}$ is the mean concentration of cells, Γ_c is the aspect ratio of the cylindrical domain used in the experiment.

r_0 (cm)	H (cm)	$\bar{n}$ (cells/cm^3)	Γ_c
2.5	0.469	1.89×10^6	5.3

TABLE II. Nondimensional parameters used in our numerical simulations. S is the Schmidt number, R is the Rayleigh number, G is the gyrotactic number, V_c is the scaled swimming velocity, and Γ is the aspect ratio of the box geometry.

S	R	G	V_c	Γ
20	955.38	7.7×10^{-3}	9.38	10

is $W_c = 100\ \mu$m/s, and the gyrotactic parameter is $B = 3.4$ s. We note that the aspect ratio $\Gamma = 10$ is for a box geometry where $\Gamma = L/H$ and L is the side length of the box. This yields a domain of similar size to those of the experiment with $\Gamma_c \approx 5$ where the aspect ratio is based upon the domain radius.

The spatial variation of the bioconvection patterns at several times during the time evolution are shown in Fig. 1. Color contours of the concentration field $n(x,y)$ are illustrated at the top surface ($z = 1$) of the suspension layer. Red (light gray) indicates a large concentration and blue (dark gray) indicates a small concentration. The time increases from panel (a) through panel (d). The pattern did not reach a steady state at long times but continued to show slow and small scale dynamics with the essential features of the pattern remaining similar to what is shown in panel (d).

We have performed numerous numerical tests to ensure that our results are not a result of the underlying spectral element grid nor a result of the particular choice of initial conditions used. We have run simulations with different spatial resolutions and also from different initial conditions and we have found

that the trends illustrated in Fig. 1 are qualitatively correct in general [30].

Figure 2 illustrates the bioconvection pattern across a vertical cross section of the domain for each of the panels of Fig. 1. The vertical cross section shown in Fig. 2 is the x-z plane that crosses through the domain shown in Fig. 1 from left to right. The exact location of the slice is chosen to be near the center of the domain and to also cut through the regions of large concentration in order to visualize the plume structure and dynamics. Color contours are shown that represent the cell concentration $n(x,z)$, with red (light gray) representing large concentrations and blue (dark gray) representing small concentrations. The arrows represent the vector for the suspension velocity **u**. Figure 2 illustrates that in regions of large concentrations the suspension velocity is downward, as indicated by the falling plume.

In our numerical simulations the suspension layer evolves from the initial conditions toward the equilibrium state where there is a dense layer of microorganisms near the top surface. Theoretically, the equilibrium state is one with zero suspension velocity and an exponential vertical variation in the concentration field [11]. The suspension layer in the numerical simulations becomes unstable before the equilibrium state is completely established. At early times the instability is strongest near the sidewalls and rapidly encompasses the entire layer. Figures 1 and 2 illustrate that the pattern that grows initially has a smaller wavelength than the pattern at long times. The central region of the domain has a relatively small suspension velocity at early times in the pattern evolution.

The general pattern evolution shown in Fig. 1 is in qualitative agreement with what has been observed in experiment, where it was found that roll-type patterns became patterns of dots at long times (for example, see Fig. 11 of Ref. [6]). A qualitative description of the pattern evolution is as follows. At short times, the microorganisms on average swim toward the upper surface and result in a larger concentration which eventually passes a critical threshold, resulting in the formation of falling plumes. These initial falling plumes are in stripe- or line-type structures, as shown in Fig. 1(a). These lines then become unstable to a pattern of dot structures that are formed in a somewhat regular array, as shown in Fig. 1(b). The dot structures then interact slowly in time to yield a final state of dots that are often connected by lines to yield starlike structures, which can be seen in Figs. 1(c)–1(d). These starlike structures then exhibit very slow dynamics that continue for the duration of our simulations. In the experiments [6], an annular pattern is observed after the dots are formed, which grows and then becomes unstable again to dots which fill most of the domain. We did not find evidence of the annular phase of the pattern evolution along the progression to the final long-term patterns in the numerical simulations.

The initial dynamics and symmetry present in the patterns of Fig. 1 suggest that the boundary conditions and the planform of the domain geometry may have a significant effect upon the dynamics. In order to explore this further, we also computed the bioconvection dynamics in a much larger domain and in domains with periodic sidewall boundary conditions. Representative results from these simulations at long times are shown in Fig. 3. Figure 3(a) is for the same geometry and conditions of Fig. 1 ($\Gamma = 10$) but with periodic boundary
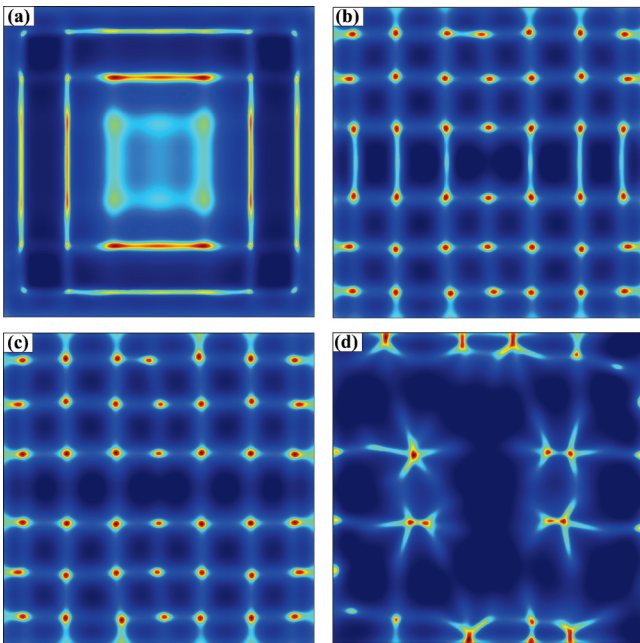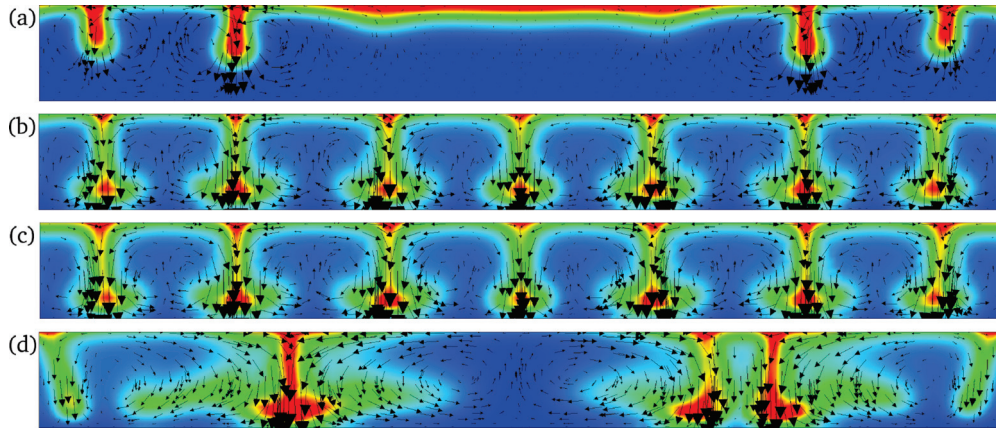

FIG. 1. (Color online) Bioconvection patterns at the top surface ($z = 1$) of a box domain with aspect ratio $\Gamma = 10$. Color contours are shown for the cell concentration n, where red (light gray) is large concentration and blue (dark gray) is small concentration. The different panels are the patterns for (a) $t = 0.24$, (b) $t = 0.5$, (c) $t = 1.25$, and (d) $t = 8$. The dimensionless parameters used are given in Table II.

FIG. 2. (Color online) The vertical structure of the bioconvection patterns for the conditions of Fig. 1. An x-z cross section is shown. Color contours are of the cell concentration n, where red (light gray) is large concentration and blue (dark gray) is small concentration. The arrows represent velocity vectors for the suspension velocity **u**. The different panels are (a) $t = 0.24$, (b) $t = 0.5$, (c) $t = 1.25$, and (d) $t = 8$. The dimensionless parameters used are given in Table II.

conditions. Figure 3(b) shows results for a large domain with an aspect ratio of $\Gamma = 40$ and periodic boundary conditions.

For the domains with periodic sidewall boundary conditions, the initial pattern emerges over the entire bioconvection layer and it is composed of domains of dots with a square latticelike-type structure. These domains of dots are similar to what is shown in Fig. 1(c); however, the domains are at different orientations with respect to each other and are separated by domain boundaries and defect structures. These initial dynamics are in contrast to the inward-propagating line structure from the lateral boundaries that then evolve into a lattice of dot structures, as seen in the simulations with rigid sidewalls at early times. Our results suggest that the initial line structures found in the simulations with rigid sidewalls are due to the planform of the geometry and the sidewall boundary conditions. However, after these initial dynamics where $t \lesssim 0.25$, the lattice of dotlike structures is a general feature of the dynamics that appears independent of the sidewall boundary conditions. We have also conducted long-time simulations in the large domain $\Gamma = 40$ with rigid sidewall boundary conditions and the long-time patterns are similar with what is shown in Fig. 3(b).

Overall, we find that the long-time patterns do not depend significantly upon the aspect ratio or the particular sidewall boundary condition used. This is evident by comparing the patterns illustrated in Figs. 1 and 3. These results suggest that our numerical simulations in a $\Gamma = 10$ domain with rigid sidewall boundary conditions are representative of the dynamics of large spatially extended domains. It would be interesting to break the symmetry of the domain and use, for example, a cylindrical geometry; however, this is not something we have explored here. In the remaining discussion we will focus our attention upon numerical results with $\Gamma = 10$ and rigid sidewalls.

Figure 4 illustrates the time evolution of the pattern wavelength. The pattern wavelength is found at each time using the structure factor in Fourier space [6,20,31]. The solid line represents the results from numerical simulation. An estimate of the order of magnitude for the time scale describing the initial growth of the pattern in the linear regime is given by the time required for a microorganism to swim from the bottom surface to the top surface. In our nondimensional units this time scale is $\tau_0 = V_c^{-1} \approx 0.1$. In light of this our simulations are for very long times. In Fig. 4 the duration of the simulation is $\tau_f = 8 = 80\tau_0$. For comparison, the typical duration of the experiments is on the order of 5 min, which corresponds approximately to a duration of $\tau_f = 6\tau_0$.

In the numerical simulation there is an initial rapid growth of the pattern dominated by structures near the sidewalls, as shown in Figs. 1(a) and 2(a). Since the measured wavelength is a global measure of the pattern, this yields the initial large spike in the value of the wavelength. After this spike the pattern has become established over the entire domain, which yields a value that describes the length scale of Fig. 1(b), which shows a fairly regular grid of 42 plumes. At this point there is a very slow coarsening process where the plumes merge and annihilate to form a pattern of starlike structures that is described by a larger length scale. This coarsening continued for the entire duration of the numerical simulation, and we did not explore the very long time limit of these pattern dynamics.

The linear stability of a suspension has been analyzed and it is insightful to compare our numerical results with these predictions. Although the analysis can include the ellipsoidal geometry of actual cells, we will present only the results for spherical cells in order to compare directly with our simulations. Pedley *et al.* [11] analyzed the stability of a uniform base state in an infinite body of fluid. The base state has a uniform concentration of cells that are all swimming vertically upwards with zero suspension velocity. For this case of an infinitely deep layer it was found that the suspension is unstable to two-dimensional disturbances larger than a critical value given by $\lambda_c = 2\pi/\sqrt{V_c G R}$. As a result, there is no critical value of the Rayleigh number, and very long wavelength two-dimensional disturbances are unstable. Furthermore, there is a wavelength of maximum growth rate given by $\lambda_m = \lambda_c (2 + (S+1)/\sqrt{S})^{1/2} > \lambda_c$, where both λ_c and λ_m decrease as $R^{-1/2}$ with increasing values of the Rayleigh number.
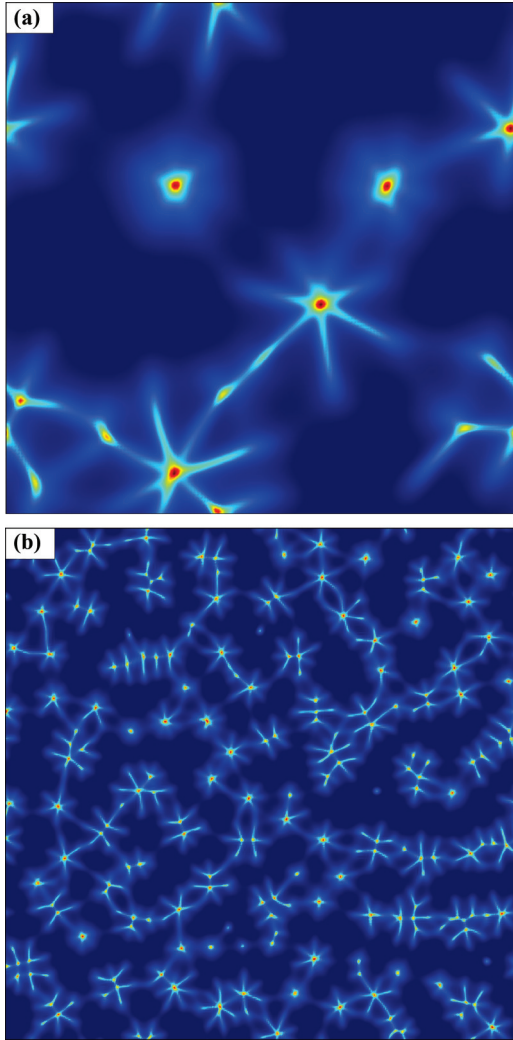
FIG. 4. Variation of the wavelength of bioconvection λ with time for $R = 955$, $S = 20$, $G = 7.7 \times 10^{-3}$, $V_c = 9.38$, and $\Gamma = 10$. The horizontal dashed lines represent the critical wavelength $\lambda_c = 0.49$, the wavelength of maximum growth $\lambda_m = 1.18$, and the long-time wavelength measured in experiment $\lambda_\infty^{\text{exp}} = 0.70 \pm 0.05$. The value shown for $\lambda_\infty^{\text{exp}}$ is the average of three different experiments where the standard deviation about the mean value is approximately 0.05. The shaded region indicates the range of wavelengths measured for the initial pattern at short times in experiment where $0.75 \leqslant \lambda_0^{\text{exp}} \leqslant 1.29$. The specific experiments used are (17)–(19) in Ref. [6].

FIG. 3. (Color online) Bioconvection patterns at the top surface ($z = 1$) of a box domain with periodic sidewall boundary conditions at time $t = 10$: (a) $\Gamma = 10$ and (b) $\Gamma = 40$. We note that panel (b) has been scaled in size by a factor of 4 in order to fit on the page. Color contours are shown for the cell concentration n, where red (light gray) is large concentration and blue (dark gray) is small concentration. The dimensionless parameters used are given in Table II.

Pedley *et al.* [11] also provide an estimate for the linear stability of a uniform layer of finite depth by allowing the finite depth to provide a cutoff for the allowable maximum wavelength of the vertical variation of the disturbance. These results are only estimates in the sense that a uniform base state does not satisfy the governing equations and the boundary conditions for a layer of finite depth. Under these approximations there is a critical Rayleigh number given by $R_c^{(u)} = 16\pi^2/V_c G$, where the notation $R_c^{(u)}$ indicates the critical Rayleigh number of a layer of finite depth starting from uniform base state. For our parameters $R_c^{(u)} = 2178 > R$, indicating that our suspension would be stable in this sense.

The linear stability analysis was extended by Hill *et al.* [12] for the case of a layer of finite depth with realistic boundary conditions. In this case the base state is the equilibrium state that has an exponentially varying concentration of cells in the vertica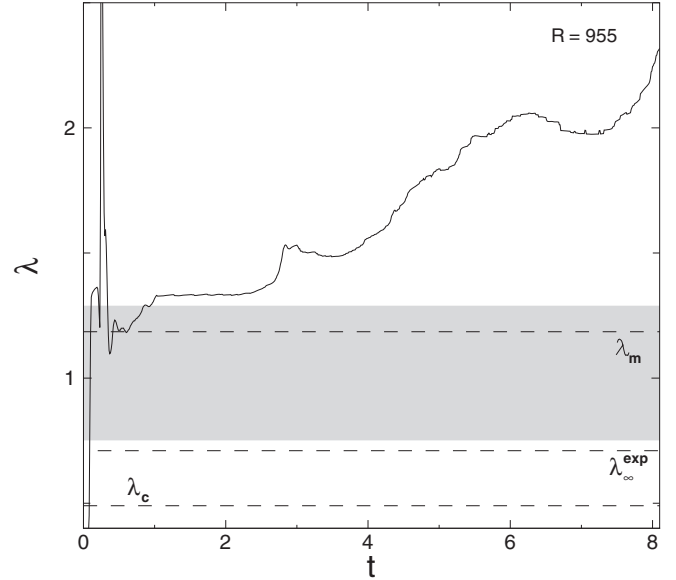l direction that satisfy the appropriate boundary conditions for a suspension of finite depth. In addition, the cells are all swimming vertically upward and there is zero suspension velocity. In Ref. [12] results were presented for the case of a rigid bottom and top surface. We computed the linear stability for our case of a rigid bottom surface and stress-free top surface using Eqs. (3.11)–(3.14) of Ref. [12].

For the parameters of Table II the results of the linear stability analysis are shown in Fig. 5. Figure 5(a) illustrates the variation of the neutral curve where the growth rate of disturbances σ is zero. This figure also yields a value for the critical Rayleigh number $R_c^{(e)} \approx 60$, where the notation (e) indicates that this is for the case of a layer of finite depth starting from the equilibrium base state. It is clear that the critical value of the wave number is zero, indicating again that the layer is unstable to long wavelength disturbances.

Figure 5(b) illustrates the variation of the growth rate σ with wave number k where $k = 2\pi/\lambda$. It can be seen that for wave numbers less than k_c the growth rate is positive. In addition, the wave number of the maximum value of the growth rate yields k_m.

Figure 4 includes horizontal lines representing several wavelengths of interest. The experimentally measured value of the wavelength at long times is represented as the dashed line at $\lambda_\infty^{\text{exp}} = 0.70 \pm 0.05$, where we have used the average value from experiments (17)–(19) in Ref. [6]. The ± 0.05 is the standard deviation about the mean value and represents the variation observed in the three different experimental measurements which began from different initial conditions. This indicates that the long-time value of the wavelength in
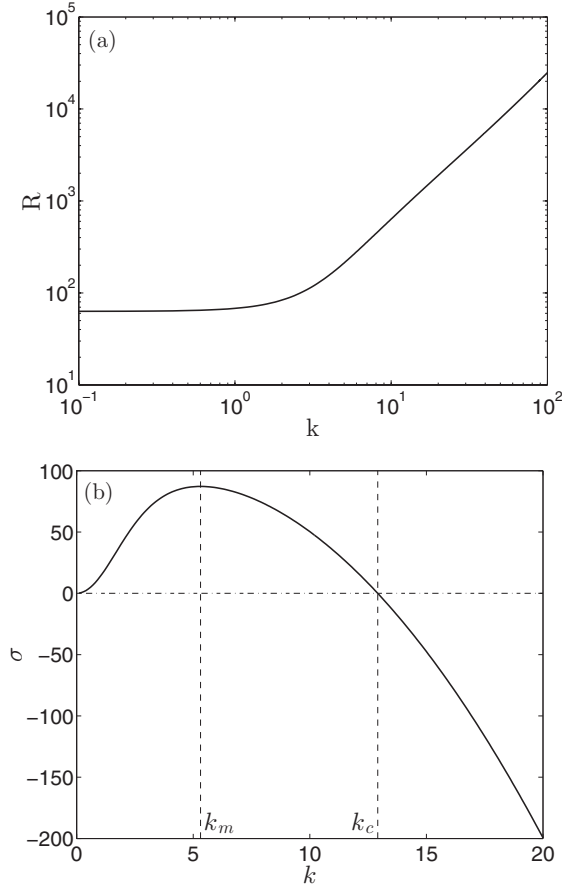
FIG. 5. Results from the linear stability analysis of a suspension of infinite horizontal extent but finite depth, where the bottom surface is rigid and the top surface is free, and the base state is given by the equilibrium state. These results are for $S = 20$, $G = 7.7 \times 10^{-3}$, and $V_c = 9.38$. (a) The neutral curve. (b) The variation of the growth rate of two-dimensional disturbances σ with the wave number k, where $k = 2\pi/\lambda$ and $R = 955$. k_c is the critical wave number in the sense that disturbances with smaller wave number are unstable. k_m is the wave number describing the disturbance with the maximum growth rate.

the experiments had little variation with the initial conditions. However, in the experiments it was reported that the short-time wavelength $\lambda_0^{\exp}$ was found to depend strongly upon the initial conditions resulting from the initial stirring of the suspension layer. The variation of the experimentally measured wavelength at short times is indicated by the shaded region where $0.75 \leqslant \lambda_0^{\exp} \leqslant 1.29$.

Our results indicate that for times $t \lesssim 3$ the wavelength of the numerical simulation is similar to the wavelength of maximum growth rate λ_m. For longer times, the nonlinear evolution of the bioconvection pattern continues to grow to larger values as the pattern coarsens into the starlike structures. The long-time wavelength of the numerical simulation is over 3 times larger than the experimentally measured value. In addition, the experimental measurements exhibit the trend where the initial pattern that is formed has a larger wavelength than the long-time pattern. However, the numerical simulations indicate that the deterministic model yields the opposite behavior where the short-time pattern (excluding

the very early transients) is of a smaller wavelength than the long-time pattern. These results suggest that although the linear regime is in agreement with the experiments, there are quantitative differences in the nonlinear long-time evolution. As a result, this suggests that the long-time wave-number selection observed in experiment may not be captured by the current form of the deterministic model.

B. Variation with Rayleigh number

There are many interesting limits of the model that one could explore using our numerical approach. However, the computations are quite expensive for spatially extended domains and in the following we have chosen to investigate the variation in the pattern dynamics with the Rayleigh number. As shown in Eq. (12), the Rayleigh number depends upon a number of parameters. However, if we consider *C. nivalis* as the microorganism of interest, the parameters that can vary are the average cell concentration $\bar{n}$ and the suspension depth H. For example, one way to increase the Rayleigh number would be to simply increase the concentration of the cells while holding the remaining variables constant. The Rayleigh number is an important parameter in determining the dynamics and is the typical control parameter used to describe convection problems. The effect of increasing the Rayleigh number results in a stronger contribution of buoyancy-induced motion relative to viscous dissipation.

In the following we have held all of the parameters constant while varying the Rayleigh number over the range $100 \leqslant R \leqslant 3000$ to cover experimentally accessible states. For all but one of our numerical simulations, $R < R_c^{(u)} = 2178$, indicating that a layer of finite thickness with a uniform base state would be stable for these conditions. We have performed one simulation with $R = 3000$, which would also be unstable to the uniform base state. For the conditions of our simulations the linear stability analysis predicts a critical value of the Rayleigh number for the equilibrium base state of $R_c^{(e)} \approx 60$. Our numerical simulation for $R = 100$ did not yield a bioconvection pattern and resulted in a stable dense layer of microorganisms at the top surface. For $R \geqslant 500$ all of our simulations did yield bioconvection patterns. It is possible that the finite size of our domain in the lateral direction affects the value of the critical Rayleigh number. In this paper we are more interested in the long-time nonlinear evolution of the patterns and did not explore this aspect in detail.

Figure 6 illustrates the long-time nonlinear evolution of the bioconvection patterns for $R = 500, 1000, 1500, 2000$ in panels (a) through (d), respectively. Our results show a transition from a pattern resembling a lattice of dots joined by lines for small values of R to a pattern composed of an irregular array of connected dots for large values of R. The red (light gray) regions of Fig. 6 represent a large concentration of the microorganisms in downward plumes.

The time variation of the pattern wavelength is shown in Fig. 7 for all of the Rayleigh numbers that have been simulated for the time range $t \lesssim 7$. Even at these late times the pattern wavelength continues to meander in time and does not appear to be approaching a steady value, except for the lowest Rayleigh number simulation at $R = 500$. The simulation at $R = 3000$ required a smaller time step and, as a result, it
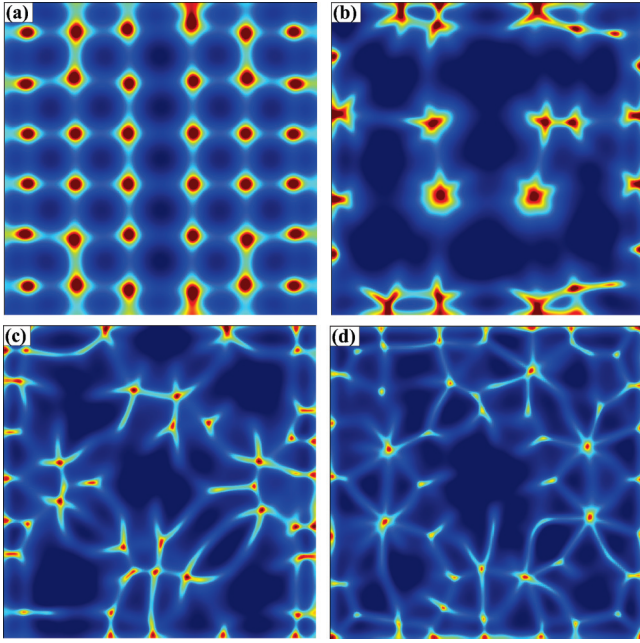
FIG. 6. (Color online) The long-time bioconvection patterns at the top surface of a box domain with aspect ratio $\Gamma = 10$ for the range of Rayleigh numbers $500 \leqslant R \leqslant 2000$. Color contours of the cell concentration n are shown at the top surface at time $t = 7$. Red (light gray) is large concentration and blue (dark gray) is low concentration, where (a) $R = 500$, (b) $R = 1000$, (c) $R = 1500$, and (d) $R = 2000$. The remaining parameters are given in Table II.

FIG. 8. (Color online) Variation of the wavelength of bioconvection λ with Rayleigh number R. The squares (red) are the long-time pattern wavelength from the numerical simulations (the patterns are shown in Fig. 6). The triangles (blue) are the short-time pattern wavelength from the numerical simulations. The dashed lines are included to guide the eye. The diamonds (cyan) and circles (green) are the experimentally measured short-time and long-tome wavelengths, respectively, from Ref. [6]. The two labeled solid lines are the critical wavelength λ_c and the wavelength of maximum growth rate λ_m that have been determined from a linear stability analysis of a finite layer with an equilibrium base state and our boundary conditions.

was only simulated until $t \approx 4$. An interesting feature of this simulation was the presence of oscillations in the dynamics; these oscillations can also be seen in the rapid time variation of the wavelength. For this case, the long-time pattern consists of starlike structures whose size oscillates slowly in time. It is also clear from our results that the long-time values of the
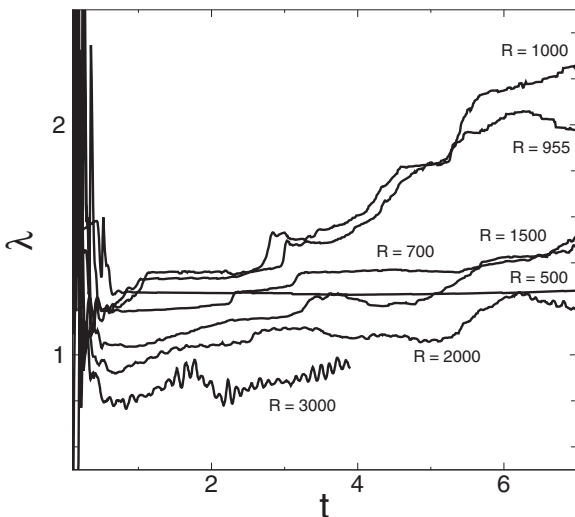
bioconvection wavelength do not follow a monotonic trend with the Rayleigh number.

The variation of the pattern wavelength with Rayleigh number is shown in Fig. 8. The squares are the long-time wavelength of the simulation measured at time $t = 7$, except for the $R = 3000$ case which was measured at $t = 4$. As previously discussed, this should not be taken as a steady value but as a representation of the scale of the magnitude at long times. The triangles are the pattern wavelength from the numerical simulation at short times. This value of the wavelength is the value just after the large initial transients shown in Fig. 7. The dashed lines are included to guide the eye. By comparing the short-time and long-time values of the wavelength, the amount of wavelength growth with the nonlinear evolution is evident. The solid lines represent the variation with Rayleigh number of the critical wavelength λ_c and the wavelength of maximum growth λ_m for the case of a finite layer starting from an equilibrium base state with our boundary conditions. It is clear that the initial pattern wavelength is quite similar to λ_m. For the case of $R = 955$ we performed three long-time simulations that started from different random initial conditions in order to quantify the variation in our wavelength results. Using these results, the standard deviation of the long-time wavelength is 0.14 and for the short-time wavelength the standard deviation is 0.06.

The circle and diamond symbols on Fig. 8 are the experimental results of Ref. [6] that have been rescaled using our conventions for nondimensionalization. The diamond symbols are the experimental pattern wavelength at early times λ_0^{exp}, and the circles are the pattern wavelength at long times $\lambda_\infty^{\mathrm{exp}}$. Although the different experiments are for different values

FIG. 7. Variation of the wavelength of bioconvection λ with time. The solid curves are numerical results for seven different values of the Rayleigh number R. The remaining simulation parameters are given in Table II.
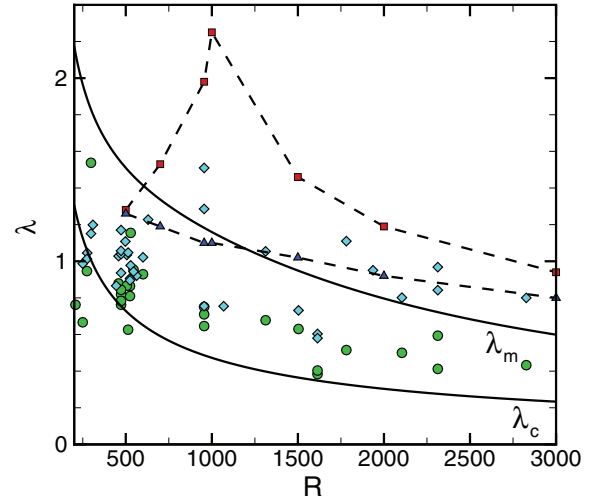
of d and G, the variation in these parameters is quite small and this provides a way to visualize the general experimental trends of the pattern wavelength with the Rayleigh number. For some values of the Rayleigh number it was not possible to experimentally measure $\lambda_\infty^{\text{exp}}$ and in these cases a value is not reported in Ref. [6].

From these results several comments can be made. Both the short-time and long-time wavelengths of the experimentally measured patterns decrease with increasing values of the Rayleigh number. It is also evident that the experimental patterns have a larger wavelength at short times which then decrease toward the long-time value. The amount of variation in the experiments of the short-time wavelengths with different initial conditions is also evident. Overall, the numerical simulations, experiment, and the linear stability analysis are in agreement for short times. However, for long times there are quantitative differences between the numerical results and the experimental measurements.

IV. CONCLUSION

We have explored numerically the continuum model of bioconvection by Pedley *et al.* [11] in spatially extended domains for long times to quantify the nonlinear pattern evolution. We have used a highly parallel, spectral-element numerical approach. In this investigation we have focused upon a box geometry with parameters appropriate to compare with the experiments of Bees and Hill [6]. We have found that the deterministic model does a remarkably good job of describing the general pattern evolution of bioconvection for the conditions of experiment. However, quantitatively there are several important differences. The experiments evolve toward smaller wavelength patterns and the numerical simulations evolve toward larger wavelength patterns. Our results suggest this model may be used, as one of the simpler choices available, to study important open questions regarding the phenomena of bioconvection in the linear regime. Our results also suggest that model modifications may be required for quantitative agreement in the long-time nonlinear regime.

There are a number of important approximations used in our numerical simulations that we would like to highlight. The experiments are in circular geometries whereas the simulations are in a box geometry. For the aspect ratios explored it is possible that the boundaries could play a significant role in the pattern evolution. The geometry of *C. nivalis* is slightly elliptical whereas we have assumed spherical cells. It is known that the elliptical nature of the geometry affects the linear stability [11,12], and this could also affect the nonlinear evolution as well. The numerical simulations are deterministic, and a more accurate representation would include the random variations of the cells and their properties, such as geometry, swimming directions, etc.

However, we emphasize that our numerical approach is quite general and can be extended as models and experiments improve to include, for example, much larger domains, deeper or more shallow chambers, different geometries such as cylindrical domains, anisotropic diffusion coefficients, etc., as well as a means to perform a more exhaustive exploration of the parameter space. An important advance that results from performing realistic numerical simulations using available nonlinear models is the ability to test hypotheses in the long-time limit, which is important experimentally yet currently inaccessible to direct theoretical analysis.

[1] T. J. Pedley and J. O. Kessler, Annu. Rev. Fluid Mech. **24**, 313 (1992).

[2] R. J. Charlson, J. E. Lovelock, M. O. Andreae, and S. G. Warren, Nature (London) **326**, 655 (1987).

[3] P. Falkowski, Nature (London) **483**, S17 (2012).

[4] S. Vogel, *Life in Moving Fluids* (Princeton University Press, New York, 1994).

[5] J. R. Platt, Science **133**, 1766 (1961).

[6] M. A. Bees and N. A. Hill, J. Exp. Biol. **200**, 1515 (1997).

[7] J. B. Loefer and R. B. Mefferd, Am. Nat. **86**, 325 (1952).

[8] S. Childress, M. Levandowsky, and E. A. Spiegel, J. Fluid Mech. **63**, 591 (1975).

[9] J. O. Kessler, Nature (London) **313**, 218 (1985).

[10] N. A. Hill and T. J. Pedley, Fluid Dynam. Res. **37**, 1 (2005).

[11] T. J. Pedley, N. A. Hill, and J. O. Kessler, J. Fluid Mech. **195**, 223 (1988).

[12] N. A. Hill, T. J. Pedley, and J. O. Kessler, J. Fluid Mech. **208**, 509 (1989).

[13] T. J. Pedley and J. O. Kessler, J. Fluid Mech. **212**, 155 (1990).

[14] N. A. Hill and D. P. Häder, J. Theo. Biol. **186**, 503 (1997).

[15] S. Ghorai and N. A. Hill, Phys. Fluids **12**, 5 (2000).

[16] S. Ghorai and N. A. Hill, Phys. Fluids **19**, 054107 (2007).

[17] M. M. Hopkins and L. J. Fauci, J. Fluid Mech. **455**, 149 (2002).

[18] M. R. Paul, K.-H. Chiam, M. C. Cross, P. F. Fischer, and H. S. Greenside, Physica D **184**, 114 (2003).

[19] M. R. Paul, K.-H. Chiam, M. C. Cross, and P. F. Fischer, Phys. Rev. Lett. **93**, 064503 (2004).

[20] M. C. Cross and P. C. Hohenberg, Rev. Mod. Phys. **65**, 851 (1993).

[21] E. Bodenschatz, W. Pesch, and G. Ahlers, Annu. Rev. Fluid Mech. **32**, 709 (2000).

[22] M. R. Paul, M. C. Cross, P. F. Fischer, and H. S. Greenside, Phys. Rev. Lett. **87**, 154501 (2001).

[23] J. D. Scheel, M. R. Paul, M. C. Cross, and P. F. Fischer, Phys. Rev. E **68**, 066216 (2003).

[24] K.-H. Chiam, M. C. Cross, H. S. Greenside, and P. F. Fischer, Phys. Rev. E **71**, 036205 (2005).

[25] A. Karimi and M. R. Paul, Phys. Rev. E **85**, 046201 (2012).

[26] M. Deville, P. Fischer, and E. Mund, *High Order Methods for Incompressible Flow* (Cambridge University Press, Cambridge, UK, 2002).

[27] Y. Maday, A. T. Patera, and E. M. Ronquist, J. Sci. Comput. **5**, 262 (1990).

[28] P. F. Fischer and J. W. Lottes, in *Domain Decomposition Methods in Science and Engineering Series*, Domain Decomposition Methods in Science and Engineering, edited by R. Kornhuber, R. Hoppe, J. Priaux, O. Pironneau, O. Widlund, and J. Xu (Springer, New York, 2004).

[29] J. W. Lottes and P. F. Fischer, J. Sci. Comput. **24**, 45 (2005).

[30] A. Karimi, Ph.D. thesis, Virginia Polytechnic Institute and State University, 2012.

[31] S. W. Morris, E. Bodenschatz, D. S. Cannell, and G. Ahlers, Phys. Rev. Lett. **71**, 2026 (1993).